Decrease of Rossby Wave Breaking Frequency over the Middle North Pacific in Boreal Summer under Global Warming in Large-Ensemble Climate Simulations

Kazuto TAKEMURA

Graduate School of Science, Kyoto University, Kyoto, Japan
Climate Prediction Division, Japan Meteorological Agency, Tokyo, Japan

Hitoshi MUKOUGAWA

Graduate School of Science, Kyoto University, Kyoto, Japan

and

Shuhei MAEDA

Aerological Observatory, Japan Meteorological Agency, Tsukuba, Japan

(Manuscript received 7 August 2020, in final form 10 March 2021)

Abstract

Future change of Rossby wave breaking (RWB) frequency over the middle North Pacific (MNP) in August and the related features of large-scale atmospheric circulation are examined using large-ensemble simulations of current and future climates with a global circulation model. Correlation analysis indicates that the RWB frequency over the MNP in the current climate can show a relationship with El–Niño Southern Oscillation as reanalysis. The RWB frequency in the future climate shows significant decreases over the MNP, compared with that in the current climate. The large-scale atmospheric circulation in the upper troposphere in the future climate indicates a significant weakening of the Asian summer monsoon circulation and the consequent southward shifted Asian jet. The decreased RWB frequency over the MNP is associated with the modulated Asian jet through reduced diffluence and deceleration of the jet in the basic state over the region. Rossby wave propagation over Eurasia and the North Pacific in midlatitudes is also clearly reduced in the future climate, consistent with the decreased RWB frequency over the MNP. The correlation and histogram analyses of the current and future experiments indicate that the significantly decreased RWB frequency over the MNP is associated with significantly suppressed convective activities east of the Philippines in the future climate. The diagnosis using ω-equation further shows the dynamical impact of the decreased RWB frequency on the suppressed convective activities through the weakened extension of the Mid-Pacific trough and the consequent weakening of dynamically induced ascent east of the Philippines.

Keywords   future change; Rossby wave; wave breaking; Asian monsoon

---

Corresponding author: Kazuto Takemura, Graduate School of Science, Kyoto University, Kitashirakawa Oiwake-cho, Sakyo, Kyoto 606-8502, Japan
E-mail: takemura.kazuto@kugi.kyoto-u.ac.jp

1. Introduction

Rossby wave propagation along the Asian jet (Lu et al. 2002; Enomoto et al. 2003) frequently causes Rossby wave breaking (RWB) east of Japan (e.g., Postel and Hitchman 1999, 2001; Abatzoglou and Magnusdottir 2006), where the Asian jet exit is located, in boreal summer. The RWB near Japan is accompanied by an equivalent barotropic structure of anticyclone, which is referred to as the Bonin high (Enomoto 2004) and causes an abnormally hot summer climate over the region. Most of the RWBs east of Japan in boreal summer are categorized as anticyclonic type (Bowley et al. 2019; Takemura et al. 2020) associated with the RWB occurrence to the south of the subtropical jet core in the basic state. The anticyclonic RWB east of Japan has impacts on enhanced convective activities to the south over the subtropical western North Pacific (WNP) through the southwestward intrusion of high potential vorticity (PV) air mass and the consequent dynamically induced ascent (Takemura et al. 2017; Takemura and Mukougawa 2020). Takemura and Mukougawa (2020) further indicated that enhanced convection over the subtropical WNP due to the RWB east of Japan can promote the Pacific–Japan (PJ) pattern (Nitta 1987; Kosaka and Nakamura 2006) accompanied by anticyclonic circulation anomalies near Japan. This polarity of the PJ pattern also corresponds to the enhanced Bonin high associated with the extended North Pacific subtropical high toward Japan and contributes to abnormally hot summer climate over the region (Wakabayashi and Kawamura 2004).

Future changes of the RWB frequency east of Japan due to long-term trend thus will be one of the essential debates to reveal the detailed process in the long-term trend of surface temperature over Japan in summer (e.g., Imada et al. 2017). de Vries et al. (2013) examined the seasonal frequency of atmospheric blocking from the North Atlantic to Europe in the future climate, indicating a significant decrease of the frequency over the North Atlantic in summer because of a northward shift of jet. Although the blocking includes not only the RWB but also "Ω"-shaped amplified ridge (Pelly and Hoskins 2003), the blocking frequency is expected to approximately correspond to the RWB frequency. For the North Pacific, Matsueda and Endo

(2017) showed unique and uncertain changes of summertime blocking frequency in the future climate, with a slight increase for the duration between 15 days and 29 days and a decrease for that between 5 days and 9 days. Takemura et al. (2020), conversely, suggested a long-term decreasing trend of the RWB frequency, which is derived from reversal of potential temperature fields at the dynamical tropopause (Pelly and Hoskins 2003), from Japan to the east in August using a dataset of the Japanese 55-year reanalysis (JRA-55; Kobayashi et al. 2015). Their suggestion motivates us to examine the future change of the RWB frequency east of Japan in more detail. The Silk Road pattern (Enomoto et al. 2003; Kosaka et al. 2009), which is a wave train associated with Rossby wave propagation along the Asian jet, frequently causes the RWB near the jet exit region (Enomoto 2004). Uchida and Kosaka (2019, 2020) indicated decreased amplitude of the Silk Road pattern in the future climate based on a principal component analysis of 200 hPa relative vorticity in summer derived from large-ensemble climate simulations. Considering the contribution of the strong Rossby wave propagation to the RWB near the Asian jet exit region (e.g., Enomoto 2004; Postel and Hitchman 1999, 2001), the result of Uchida and Kosaka (2019, 2020) implies a possibility of a decrease in RWB frequency east of Japan in the future climate. The future change of the RWB frequency east of Japan, conversely, has not been examined yet.

Meanwhile, the future change of atmospheric circulation in the tropical WNP has been an ongoing debate in previous studies. Kosaka and Nakamura (2011) showed, from multi-model ensemble simulations, a reduced occurrence of the PJ pattern with cyclonic (anticyclonic) circulation anomalies around the Philippines (Japan) under the climatologically suppressed convective activity over the tropical WNP in the future climate. Yoshida et al. (2017) and Sugi et al. (2020) indicated a decreased number of tropical cyclones and their seeds over the tropical WNP in a future climate, which is consistent with the suppressed convective activities over the tropical WNP.

On the basis of the aforementioned results, this study assesses the future change of the RWB frequency east of Japan and the related large-scale atmospheric circulation from low to middle latitudes in boreal

summer, using results of high-resolution experiments with large-ensemble historical and future climate simulations. This line of investigation is expected to contribute to the risk management of increased heatwave episodes in boreal summer resulting from ongoing global warming (Imada et al. 2019) and the associated socioeconomic decision making.

2.   Dataset and methods

To examine the future change of the RWB frequency east of Japan and the associated features of atmospheric circulation, the results of the large-ensemble climate simulation in August, which are referred to as the "Database for Policy Decision-Making for Future Climate Change" (d4PDF; Mizuta et al. 2017), for historical and future global climates are diagnosed. The daily dataset used has a grid interval of 2.5° and 24 pressure levels (top at 0.5 hPa). The numerical simulations are performed using the atmospheric general circulation model (MRI-AGCM3.2) developed by the Meteorological Research Institute (Mizuta et al. 2012). The model has a horizontal resolution of a triangular truncation of 319 with a linear Gaussian grid ($T_L 319$), which corresponds to a grid interval of approximately 55 km, and 64 vertical levels with the top at 0.01 hPa. The historical climate simulations (hereafter referred to as "current experiment") were forced by the monthly averaged historical sea surface temperature (SST) and sea ice based on COBE-SST2 (Hirahara et al. 2014) with historical anthropogenic forcing such as greenhouse gases and natural forcing. The current experiment has 100 ensemble members with different atmospheric initial perturbations and perturbed SSTs as the boundary condition, which was integrated for the 60 year period from 1951 to 2010. The future climate simulations (hereafter referred to as "future experiment") were forced by six warming patterns of SST in the future climate, which are projected using multiple models based on phase 5 of the Coupled Model Inter-comparison Project (CMIP5). The future experiment simulates 4 K warmer global mean surface air temperature than the preindustrial climate, which corresponds to a warming level at 2090 according to the representative concentration pathway 8.5 scenario of the CMIP5. The future experiment has a total of 90 ensemble members with the same initial perturbations as the current experiment, which was integrated for the 60 year period from 2051 to 2110. Here, the boundary conditions of SSTs in the future experiment are those in the current one after detrended, and the climatological SST warming pattern is added, showing the same interannual variability of

the SSTs between the current and future experiments. Further detail for each type of the climate simulations is described in Mizuta et al. (2017). A difference in the 60 year climatology of the ensemble means between the future experiment and the current experiment is referred to as "future change" in this study. The future change thus represents a shift of the climatological mean without modulations in the interannual variability of SST such as El–Niño Southern Oscillation (ENSO).

Vertical motion including convective activities in tropics is estimated using vertical p-velocity (ω) at 500 hPa. To verify this estimation, we also used the monthly mean dataset of interpolated outgoing longwave radiation (OLR) (Liebmann and Smith 1996) in August, which was provided by the U.S. National Oceanic and Atmospheric Administration. The climatology of OLR is defined as the 30 year monthly averages from 1981 to 2010.

To assess reproducibility for interannual variability of the RWB frequency east of Japan in the climate simulations, we used daily datasets of the JRA-55 (Kobayashi et al. 2015) in August during the 61 year period from 1958 to 2018. The JRA-55 system has a horizontal resolution of $T_L 319$, and we used the data interpolated to 1.25° horizontal resolution and 37 pressure levels (top at 1 hPa). To assess the reproducibility of relationships between the RWB frequency in the climate simulations and the ENSO, the 5 month running mean SST deviation for Niño-3 index (Tokyo Climate Center 2020), which is defined as areal-averaged SST over the area of (5°S−5°N, 150−90°W), is used. Here, the SST deviation is defined as a deviation from the latest sliding 30 year average.

To examine the diffluence and deceleration of basic flow near the Asian jet exit region, which is a preconditioning of the RWB (Colucci 2001), stretching deformation (d_B) of the basic state was calculated from the horizontal wind as follows:

$$d_B \equiv \frac{\partial u_B}{\partial x} - \frac{\partial v_B}{\partial y}, \tag{1}$$

which is defined according to Mak and Cai (1989) and Bluestein (1992). Here, the subscript B denotes the basic state defined by zonal wavenumbers $k \leq 3$ to exclude flows due to the Rossby waves. The diffluent and decelerated basic flow thus corresponds to negative d_B, and is generally seen over the region near or upstream of the RWB (e.g., Colucci and Alberta 1996; Colucci 2001), contributing to trigger the RWB occurrence.

To calculate the RWB frequency, we used a daily dynamical blocking index (Pelly and Hoskins 2003)
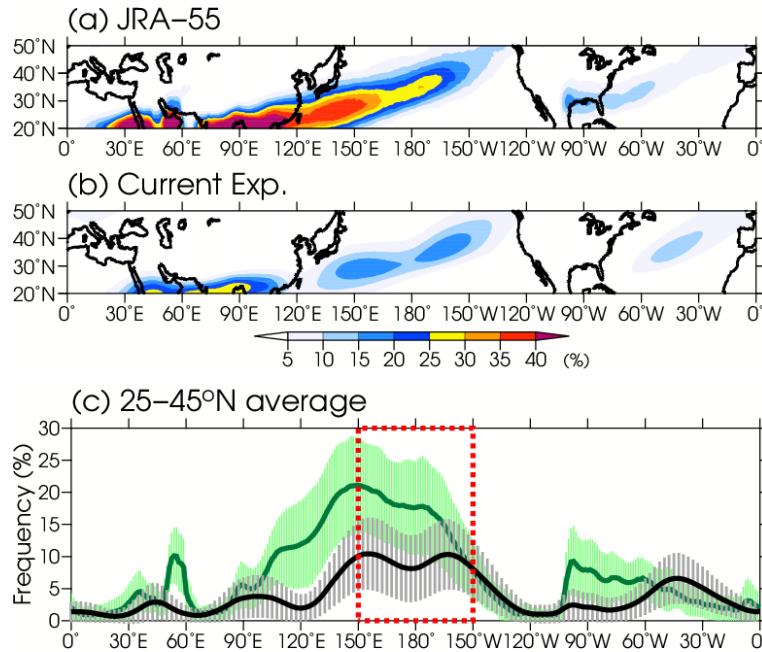
Fig. 1.   RWB frequency (%) in (a) JRA-55 and (b) current experiment (ensemble mean) and (c) that averaged over 25–45°N in August during the 53 year period from 1958 to 2010. The black and green lines in (c) indicate the RWB frequency in the current experiment (ensemble mean) and JRA-55, respectively. The gray and light green bars denote the standard deviations for interannual variability of each RWB frequency for the current experiment (all ensemble members) and the JRA-55 during the 53 year period, respectively. The red dashed rectangle in (c) denotes the area of MNP defined as the longitudinal area from 150°E to 150°W.

on the basis of meridional distributions of potential temperature θ on the dynamical tropopause defined by 2 PV units (PVU; 1 PVU = 10^{-6} K kg^{-1} m^2 s^{-1}), which is conserved without diabatic processes. The blocking index B (unit: K) is expressed as follows:

$$B = \frac{1}{\Delta\lambda} \int_{-\Delta\lambda/2}^{\Delta\lambda/2} \left[\frac{2}{\Delta\phi} \left(\int_{\phi_0}^{\phi_0+\Delta\phi/2} \theta d\phi - \int_{\phi_0-\Delta\phi/2}^{\phi_0} \theta d\phi \right) \right] d\lambda,$$
(2)

where λ is the longitude, $\Delta\lambda$ is the width of zonal average, ϕ is the latitude, $\Delta\phi$ is the typical meridional scale of the wave breaking, and ϕ_0 is the central latitude. We defined $\Delta\lambda$ as 5° and $\Delta\phi$ as 30°, respectively, according to Pelly and Hoskins (2003). A daily RWB is detected when B has a positive value: there is high θ to the north and low θ to the south. We defined monthly RWB frequency as the fraction of days for which the RWB is detected in the month, as in Takemura et al. (2020).

The propagation of quasi-stationary Rossby wave packets is analyzed using the wave activity flux (WAF) defined by Takaya and Nakamura (2001). The horizontal WAF is defined as follows:

$$W = \frac{1}{2|U|} \begin{bmatrix} \bar{u}(\psi_x'^2 - \psi'\psi_{xx}') + \bar{v}(\psi_x'\psi_y' - \psi'\psi_{xy}') \\ \bar{u}(\psi_x'\psi_y' - \psi'\psi_{xy}') + \bar{v}(\psi_y'^2 - \psi'\psi_{yy}') \end{bmatrix},$$
(3)

where u is the zonal wind, v is the meridional wind, U is the climatological horizontal wind vector, and ψ is the stream function. The overbars (primes) denote the basic states (perturbations), defined as the 60 year climatology (anomaly from the 60 year climatology). The subscripts x and y denote the partial derivatives concerning longitude and latitude, respectively. The WAF is derived from the 5 day running mean anomalies and climatology.

3.   Reproducibility of interannual variability of RWB frequency

In this section, we describe a reproducibility of the RWB frequency, focusing on the interannual variability and its relationship with the ENSO. Figure 1 first shows the RWB frequency in August during the 53 year period from 1958 to 2010 for the reanalysis (JRA-55) and the current experiment. Although the RWB frequency in both the reanalysis (Fig. 1a) and
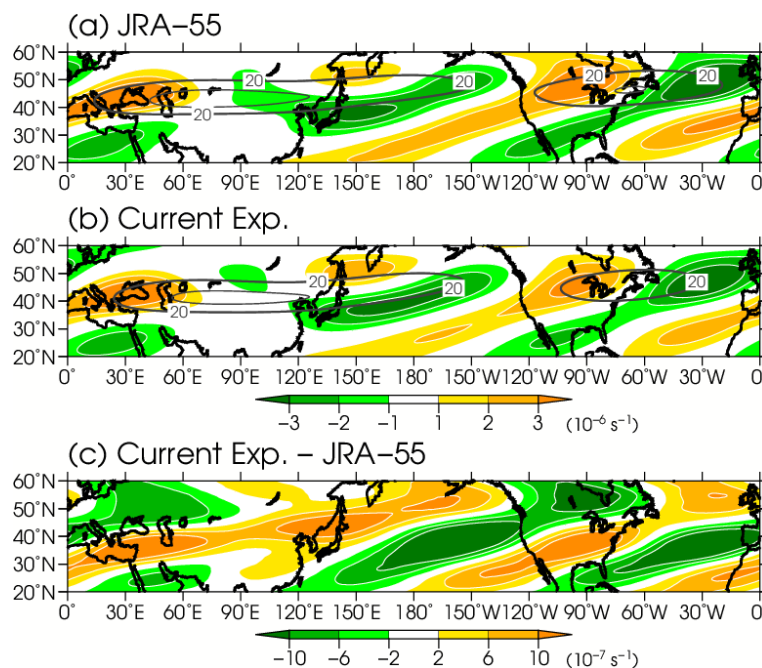
Fig. 2.   Stretching deformation (shading; unit: 10^{-6} s^{-1}) and zonal wind (contour; unit: m s^{-1}) of the basic state (zonal wavenumbers $k \leq 3$) at 200 hPa in (a) JRA-55 and (b) current experiment (ensemble mean) in August during the 53 year period from 1958 to 2010. Contours intervals in (a) and (b) are 5 m s^{-1} exceeding 20 m s^{-1}. Shading in (c) indicates the difference in the 200 hPa stretching deformation of the basic state (unit: 10^{-7} s^{-1}) between the current experiment and the JRA-55 [i.e., (b) minus (a)].

the current experiment (Fig. 1b) attains their maxima over the North Pacific, the center of the maximum in the current experiment slightly shifts eastward compared with that in the reanalysis. The smaller RWB frequency in the current experiment will be described later in Fig. 1c. There is another maximum of the RWB frequency from North America to the North Atlantic, also showing a clear eastward shift of the maximum in the current experiment compared with the reanalysis. The large RWB frequency from the eastern part of North Africa to South Asia south of 25°N (Figs. 1a, b) corresponds to the meridional overturning of the potential temperature on the 2-PVU surface, where the climatological Tibetan high is located to the north. The large climatological RWB frequency in the low-latitudes is out of scope in this study.

To highlight the RWB frequency in midlatitudes, Fig. 1c shows the RWB frequency averaged over the latitudinal band of 25−45°N. Here, the RWB frequency in the current experiment (black line in Fig. 1c) represents the ensemble mean. Although the RWB frequency in the current experiment attains its local maximum over the North Pacific as in the reanalysis (green

line in Fig. 1c), the simulated RWB frequency is approximately half of the reanalysis counterpart over the region. The underestimated RWB frequency is also seen over North America. The eastward shifted RWB frequency in the current experiment is also clear by comparing Figs. 1a and 1b. Scaife et al. (2010, 2011) indicated from their sensitive experiments that the underestimated frequency of the atmospheric blocking in the numerical models, compared with a reanalysis, is primarily due to large-scale climatological mean bias of atmospheric fields and SSTs in the models rather than the horizontal resolution. de Vries et al. (2013), who indicated the significant future decrease of the RWB frequency over the North Atlantic, also noted the underestimation of the blocking frequency over the region.

To examine environmental atmospheric circulations in the upper troposphere associated with the underestimated and eastward shifted RWB frequency over the North Pacific, stretching deformation and zonal wind at 200 hPa of the basic state (zonal wavenumbers $k \leq 3$) for the current experiment and the reanalysis are shown in Figs. 2a and 2b. The distributions of the
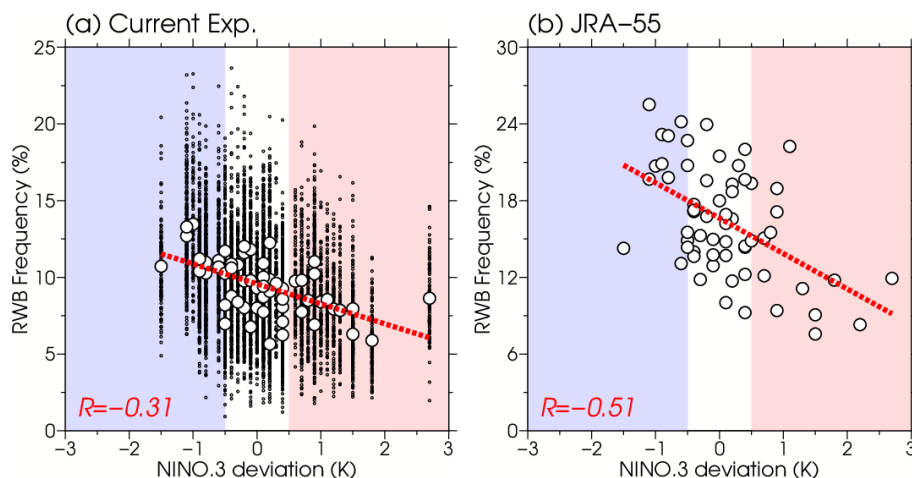
Fig. 3.   Scatter diagrams between 5 month running mean Niño-3 indices (unit: K; horizontal axis) and RWB frequen-
cy (unit: %) averaged over the MNP (25−45°N, 150°E−150°W) (vertical axis) in August. The diagrams in (a) and
(b) indicate the current experiment (all ensemble members; dots) and JRA-55 (opened circles), respectively. The
opened circles in (a) denote the ensemble mean. Statistical period in (a) and (b) is during the 60 year period from
1951 to 2010 and the 61 year period from 1958 to 2018, respectively. The correlation coefficients (R) between the
5 month running mean Niño-3 indices and the RWB frequency of (a) all the ensemble members, (b) the JRA-55
are shown at the bottom left. Red dashed lines denote their regression lines. Red and blue shadings denote the 5
month running mean Niño-3 indices higher than +0.5 K and lower than −0.5 K, which are some of the criteria for
El Niño and La Niña, respectively.

upper-level zonal wind fields and stretching deforma-
tion from Eurasia to the North Pacific in the reanalysis
are generally reproduced in the current experiment
(Figs. 2a, b). The detailed structure of the upper-
level stretching deformation in the current experiment
over the region (shading in Fig. 2b), by contrast, is
different from that in the reanalysis (shading in Fig.
2a) associated with slight differences of the horizontal
wind fields: the upper-level stretching deformation in
the current experiment is weaker from Japan to the
east and extends eastward over the midlatitude North
Pacific. The upper-level stretching deformation for
the current experiment and the reanalysis also clearly
shows the positive and negative differences over the
western and central to eastern parts of the midlatitude
North Pacific (Fig. 2c), respectively, corresponding
to the underestimated and eastward shifted RWB
frequency in the current experiment (Fig. 1c). Al-
though these results suggest that the underestimated
and eastward shifted RWB frequency is expected to
be primarily due to the climatological mean bias of
the atmospheric fields, further investigation for the
associated detailed factors will be needed. Although
the bias of the RWB frequency will have some quan-
titative impacts on its future change as noted by de
Vries et al. (2013), its relative change from the current

climate to the future climate in a single climate model,
which will be presented in this study, has validity to
be investigated.

    Bowley et al. (2019) indicated a statistically close
relationship between the anticyclonic RWB frequency
over the North Pacific and the ENSO. Takemura et al.
(2020) also statistically indicated that the anticyclonic
RWB is dominant from Japan to the east in August and
showed a significant increase of the RWB frequency
over the region during La Niña years. They further
showed the related process that an enhanced Walker
circulation and the consequent northward shift of the
Asian jet associated with the La Niña condition can
contribute to the frequent RWB from Japan to the east.
According to their results, the reproducibility of rela-
tionships between the RWB frequency averaged over
the middle North Pacific (25−45°N, 150°E−150°W;
hereafter referred to as "MNP") and the ENSO is
assessed. Figure 3 shows scatter diagrams between
the Niño-3 indices and the RWB frequency averaged
over the MNP. The RWB frequencies in both all
ensemble members of the current experiment (dots
in Fig. 3a) and the reanalysis (opened circles in Fig.
3b) show relationships with the Niño-3 indices with
negative correlation coefficients of −0.31 and −0.51,
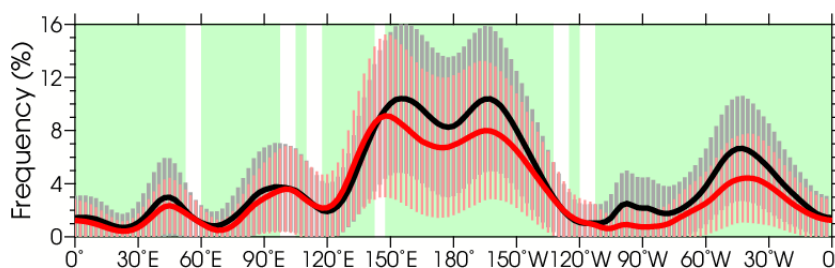respectively. The RWB frequency of the ensemble

Fig. 4.   RWB frequencies (%) averaged over 25−45°N in August for current and future experiments during the 60 year period from 1951 to 2010 and from 2051 to 2110, respectively. The black and red lines indicate the ensemble mean RWB frequencies in the current and future experiments, respectively. The gray and light red bars denote the standard deviations for interannual variability of each RWB frequency for all ensemble members in the current and future experiments during the 60 year period, respectively. The green shadings denote the longitudinal area where future changes of the RWB frequency are significant with a confidence level of 95 %.

mean in the current experiment and the Niño-3 indices (opened circles in Fig. 3a) have a stronger relationship with a negative correlation coefficient of −0.57. The ensemble mean extracts variability externally forced by SST and sea ice, indicating that atmospheric internal variability represented by all ensemble members can obscure the relationship to the ENSO. These negative correlations indicate the relationship between the RWB frequency over the MNP and the ENSO, consistent with the results of Bowley et al. (2019) and Takemura et al. (2020). It shows that responses of the RWB frequency to the ENSO, which is one of the most dominant interannual climate variabilities, are seen in the current experiment (Fig. 3a), suggesting the reproducibility for the component of interannual variation. The aforementioned results also imply that the responses of the RWB frequency to the future change can be investigated.

4.   Future change of RWB frequency and large-scale atmospheric circulation

This section describes the future change of the RWB frequency over the MNP and the associated modulation of large-scale atmospheric circulation. Figure 4 shows the RWB frequencies averaged over 25−45°N in August for the current and future experiments. The decrease in RWB frequency over the MNP is significant in the future climate (red line in Fig. 4), compared with the current one (black line in Fig. 4). The areal average of RWB frequency over the MNP decreases by more than 20 % in the future climate. The RWB frequency also shows decreasing tendencies over a wide area in the latitudinal band of 25−45°N, and the decreased frequency over the North Atlantic is consistent with the result of de Vries et al. (2013). The

RWB frequency in the midlatitudes shows increasing tendency west of the MNP near 120−140°E only, although the change of the RWB frequency is not large. The following subsections show noteworthy features of the modulated large-scale atmospheric circulations in the future climate, in association with the decreased RWB frequency over the MNP.

4.1   Large-scale tropical divergence in the upper troposphere and the Asian jet

Figure 5a shows the future change of 200 hPa velocity potential in August. In the upper troposphere, a large-scale divergence from South to Southeast Asia is significantly weakened, indicating suppressed Asian monsoon circulation in the future climate, consistent with the results of Sugi et al. (2002), Hirahara et al. (2012). The future change of velocity potential with zonal wavenumber 1 (shading in Fig. 5a) also indicates a weakened Walker circulation, compared with the current climate (contour in Fig. 5a), showing an El Niño-like atmospheric response in the tropics.

To examine the influence of the tropical circulation on the Asian jet in the future climate, the future change of 200 hPa zonal wind is shown in Fig. 5b. The future change of the upper-level zonal wind shows a significant meridional dipole pattern with westerly and easterly changes to the south and north of the jet core over Eurasia, indicating a southward shift of the Asian jet in the future climate. To further assess features of the Asian jet of the basic state (zonal wavenumbers $k \leq 3$), the future changes of 200 hPa zonal wind of the basic state from central Eurasia to the North Pacific in August are also shown in Fig. 5c. The southward shifted Asian jet core is seen in the future climate (red contour in Fig. 5c), compared with
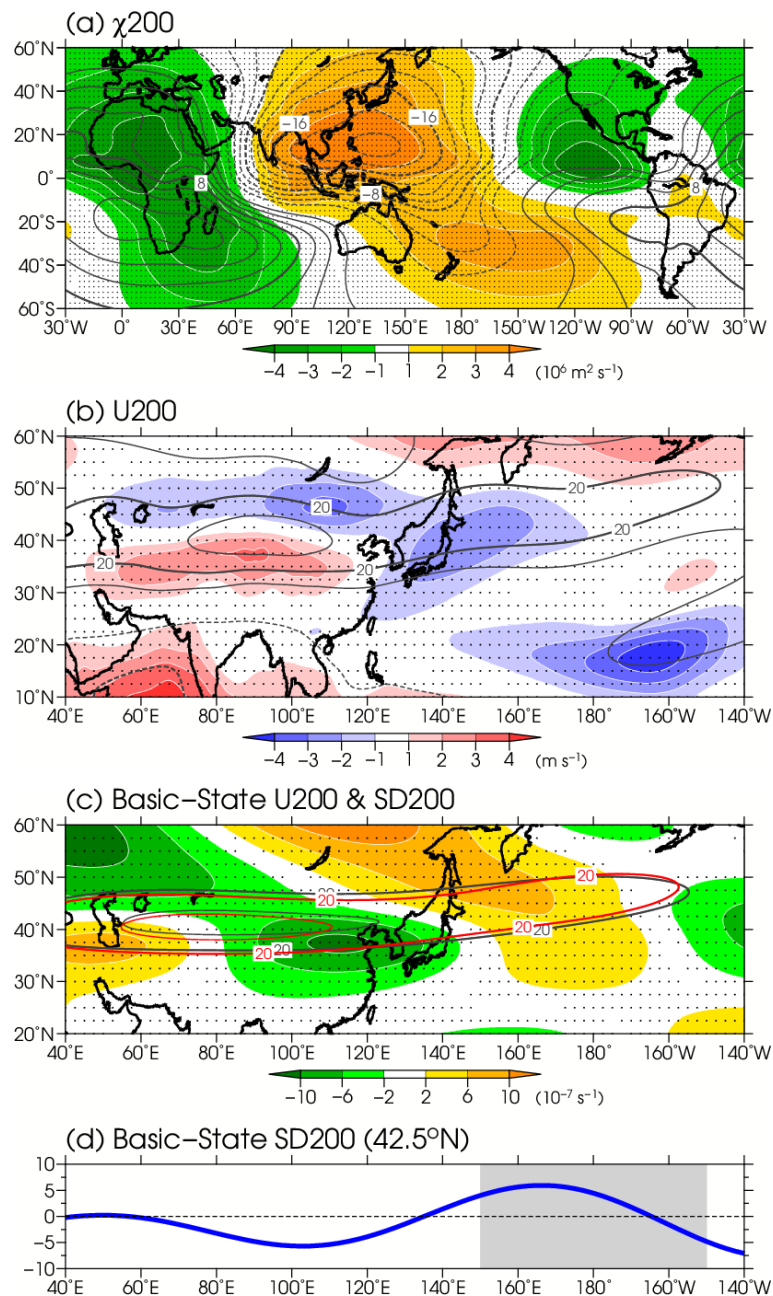
Fig. 5.   Future changes of (a) velocity potential (unit: 10^6 m^2 s^{-1}), (b) zonal wind (unit: m s^{-1}), (c) stretching deformation of the basic state (zonal wavenumbers $k \leq 3$) (unit: 10^{-7} s^{-1}) at 200 hPa (shading) and (d) its longitudinal profile along 42.5°N (blue line) in August. Contours indicate (a) the 200 hPa velocity potential with the interval of 2×10^6 m^2 s^{-1}, (b) 200 hPa zonal wind with the interval of 10 m s^{-1} in the current experiment, and (c) 200 hPa zonal wind of the basic state exceeding 20 m s^{-1} in the current (black) and future (red) experiments with the contour interval of 5 m s^{-1}. Dots denote the significant change of (a) the velocity potential, (b) the zonal wind, and (c) the planetary-scale stretching deformation at 200 hPa for all ensemble members of each experiment, with a confidence level of 95 % based on Welch's t-test. The gray shading in (d) shows the longitudinal area of the MNP (150°E–150°W).

the current climate (black contour in Fig. 5c), associated with the suppressed Asian monsoon circulation.

To further investigate the vertical structure of the Asian jet, the latitude–pressure cross-section of the future change of zonal wind of the basic state averaged over 60–120°E is shown in Fig. 6. The center of the Asian jet in the future climate (red contour in Fig. 6) clearly shifts not only southward but also upward compared with that in the current climate (black contour in Fig. 6). The future change of the zonally averaged zonal wind (shading in Fig. 6) also indicates the significantly upward-shifted Asian jet. The upward displacement of the Asian jet core is consistent with that reported by Lorenz and DeWeaver (2007), who indicated the elevated tropopause height and zonal mean–zonal wind response to the warmer climate. Notably, the southward shifted Asian jet (Figs. 5b, c) is inconsistent with the northward shift of zonal mean–zonal wind in the warmer climate described by Lorenz and DeWeaver (2007).

To focus on the influence of the suppressed Asian monsoon circulation on the southward shifted Asian jet in the future climate, Fig. 7a shows the future change of absolute vorticity at 200 hPa. The upper-level absolute vorticity clearly indicates positive (cyclonic) changes along a zonally elongated strong gradient of absolute vorticity, corresponding to the southward shifted Asian jet (Figs. 5b, c). To assess a contribution of the suppressed upper-level divergence from South to Southeast Asia to the southward shifted Asian jet, the future change of the absolute vorticity advection by horizontal divergent wind at 200 hPa is shown in Fig. 7b. Here, the absolute vorticity advection due to the divergent wind (S_χ) is defined as follows:

$$S_\chi = -\overline{\boldsymbol{v}_\chi} \cdot \nabla(\overline{\zeta} + f), \qquad (4)$$

where $\boldsymbol{v}_\chi = (u_\chi, v_\chi)$ is the horizontal divergent wind vector and ζ and f are the relative and planetary vorticity, respectively. The overbars denote the 60 year monthly climatology in each climate simulation. The shading of Fig. 7b clearly shows positive vorticity tendencies along the Asian jet, particularly over the eastern part, corresponding to the positive change of the upper-level absolute vorticity (Fig. 7a). The positive vorticity tendencies are associated with the weakened northward divergent wind (vectors in Fig. 7b) resulting from the suppressed upper-level divergence from South to Southeast Asia (Fig. 5a), indicating their contributions to the southward shifted Asian jet in the future climate. The southward shifted Asian jet shown in Figs. 5b and 5c further corresponds
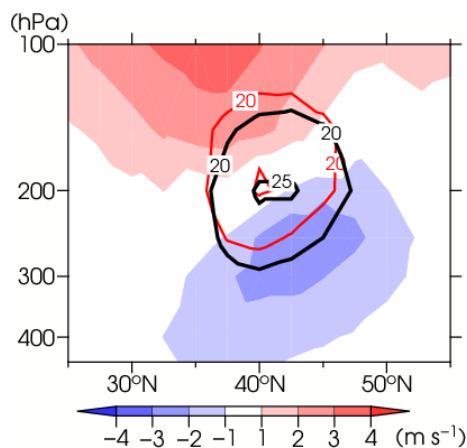

Fig. 6. Latitude–pressure cross-section of future change of zonal wind of the basic state (zonal wavenumbers $k \leq 3$) averaged over 60–120°E in the upper troposphere (shading). Contours indicate the zonally averaged zonal wind exceeding 20 m s^{-1} in the current (black) and future (red) experiments with the contour intervals of 5 m s^{-1}. Color shading denotes the future change of the zonal wind, which is significant with a confidence level of 95 %.

to the weakened extension of the Tibetan high, which is also closely associated with the suppressed Asian monsoon circulation (e.g., Sooraj et al. 2015). The southward shifted Asian jet is consistent with the result of Hirahara et al. (2012) and Horinouchi et al. (2019), who suggested that the Asian jet core would shift southward in the future climate in summer, from results of climate simulations on the basis of CMIP3 and CMIP5, respectively.

The upper-level absolute vorticity advection by the divergent wind (Fig. 7b) also shows positive changes from Japan to the east, which have opposite signs to the change of the upper-level absolute vorticity (Fig. 7a). The absolute vorticity advection by the rotational wind in the upper troposphere, which includes the horizontal vorticity advection and β effect, shows clear negative vorticity tendencies from Japan to the east (not shown), canceling and inverting the positive change of absolute vorticity advection by the divergent wind (Fig. 7b), and corresponding to the change of the upper-level absolute vorticity (Fig. 7a).

4.2 Modulated Asian jet, Rossby wave activity, and decreased RWB frequency

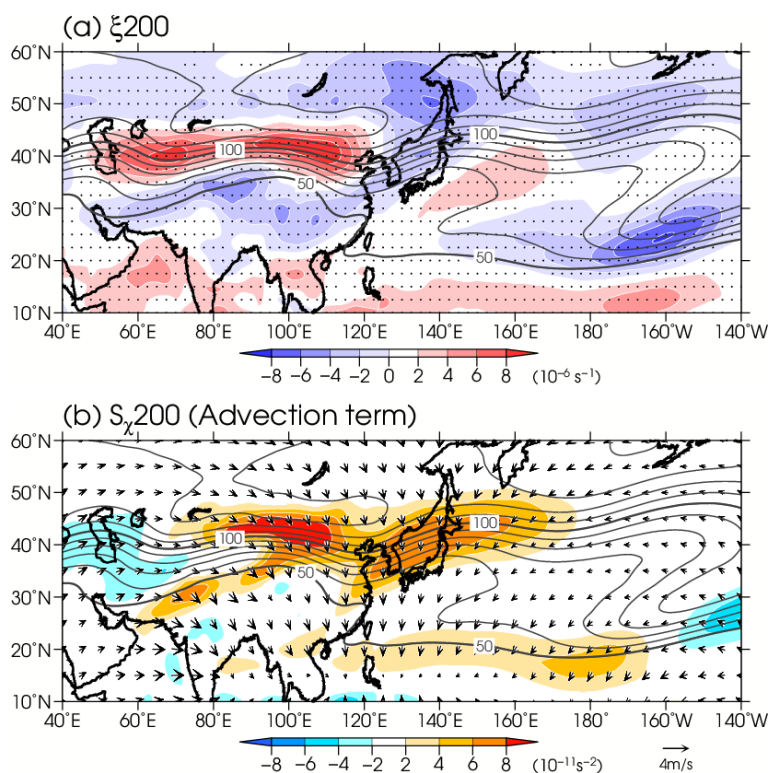To assess the influence of the modulated Asian jet on the decreased RWB frequency in the future

Fig. 7. Same as Fig. 5 but for (a) absolute vorticity (unit: 10^{-6} s^{-1}) and (b) horizontal advection of the absolute vorticity (unit: 10^{-11} s^{-2}) by divergent wind, at 200 hPa. Contours indicate absolute vorticity in the current experiment with intervals of 10×10^{-6} s^{-1}. Vectors in (b) denote the future change of 200 hPa divergent wind (unit: m s^{-1}).

climate, the future change of 200 hPa stretching deformation of the basic state described in Eq. (1) is shown as shading in Fig. 5c. A negative change of the stretching deformation is significantly seen over East Asia. The increased jet diffluence and deceleration over East Asia are associated with a slight westward shift of the Asian jet exit region at 200 hPa level in the future climate, compared with the current one (see contour lines of 25 m s^{-1} in Fig. 5c). The negative change of the stretching deformation further corresponds to the region with the increasing tendency of the RWB frequency near 120–140°E (Fig. 4), indicating a relationship between the modulated Asian jet and the increased RWB frequency over East Asia in the future experiment. By contrast, a positive change of the stretching deformation is significantly seen near the MNP, indicating a contribution of reduced diffluence and deceleration to the decrease in the RWB frequency over the MNP. The reduced diffluence and deceleration may be associated with the above-mentioned westward shift of the Asian jet exit region. The longitudinal profile for the future change of the

stretching deformation along 42.5°N (Fig. 5d), which corresponds to a latitude near the Asian jet core, also represents the positive change near or upstream of the MNP, indicating the relationship with the decrease in the RWB frequency over MNP. To further examine the relationship of the RWB frequency over the MNP and the variability of the jet diffluence and deceleration fields, the 200 hPa stretching deformation of the basic state regressed onto the RWB frequency over the MNP for the current experiment is shown in Fig. 8a. The regressed anomalies, which are scaled to the magnitude of future change in the RWB frequency over the MNP, indicate that a significantly positive stretching deformation east of Japan is related to the decreased RWB frequency over the MNP. The amplitude of the regressed stretching deformation is comparable with that of the future change (Fig. 5c). The longitudinal profile for the regressed stretching deformation along 42.5°N (Fig. 8b) also shows the relationship between the positive change of the stretching deformation near or upstream of the MNP and the decrease in the RWB frequency over the MNP. It is noteworthy that the
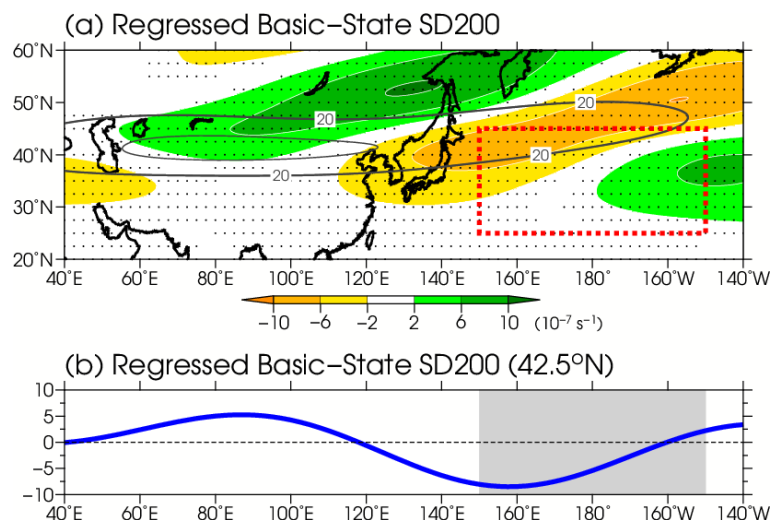
Fig. 8.   (a) Stretching deformation (shading; unit: 10^{-7} s^{-1}) of the basic state (zonal wavenumbers $k \le 3$) at 200 hPa regressed onto the areal average of RWB frequency over the MNP (red dashed rectangle) and (b) its longitudinal profile along 42.5°N (blue line). The regressed pattern is derived from the interannual variability of all ensemble members in the current experiment and is normalized by the future change of the RWB frequency over the MNP. To highlight the features of stretching deformation associated with the decreased RWB frequency, the order of colors for the shading is reversed from those in Fig. 5c. Dots in (a) denote the statistical significance of the regression with a confidence level of 95 % based on t-test. The gray shading in (b) shows the longitudinal area of the MNP. Contour denotes 200 hPa zonal wind of the basic state exceeding 20 m s^{-1} in the current experiment with the interval of 5 m s^{-1}.

amplitude of the regressed profile is almost the same as the future change (Fig. 5d) with their opposite sign, suggesting that the decrease in RWB frequency can be explained by the reduced diffluence and deceleration. These results indicate that the modulated Asian jet is closely associated with the decreased RWB near the jet exit region in the future climate.

Uchida and Kosaka (2019) indicated a reduced amplitude of the Silk Road pattern in the future climate using the large-ensemble climate simulations, as described in Section 1. Uchida and Kosaka (2020) further suggested contributions of the reduced wave energy from the upstream, which is due to the southward shifted Asian jet and a decreased blocking frequency over Europe, to the decreased amplitude of the Silk Road pattern. To examine the future change of the Rossby wave propagation from Eurasia to east of Japan, the 60 year climatology of the horizontal component of daily WAF at 200 hPa in August is shown in Fig. 9. Here, the daily WAFs are derived from the 5 day running mean fields of all ensemble members. From a comparison in the zonal component of WAF between the current and future climate (shadings in Figs. 9a, b), weakened eastward propagations of the

Rossby wave packets are seen over Eurasia and the North Pacific. To more clearly describe their difference, the future change of the climatological WAFs is shown in Fig. 9c. The future change clearly indicates the weakened Rossby wave propagation from Eurasia to the North Pacific, except near 120°E. The weakened Rossby wave propagations over Eurasia and the North Pacific are consistent with the decreased amplitude of the Silk Road pattern (Uchida and Kosaka 2019, 2020) and the decreased RWB frequency over the MNP (Fig. 4) in the future climate, respectively. The future change of the WAF also shows an enhanced northward wave emanation near 120°E, contributing to an enhancement of Rossby wave propagation north of 50°N to the east, contrary to the weakened propagation over the midlatitude North Pacific. The enhanced northward wave emanation near 120°E further corresponds to the region where the increased jet diffluence and deceleration at 200 hPa over East Asia (Fig. 5c) and the associated increase of the RWB frequency near 120–140°E (Fig. 4) are seen.

These results suggest that the modulated Asian jet can contribute to the reduced Rossby wave activity over the midlatitude North Pacific and the consequent
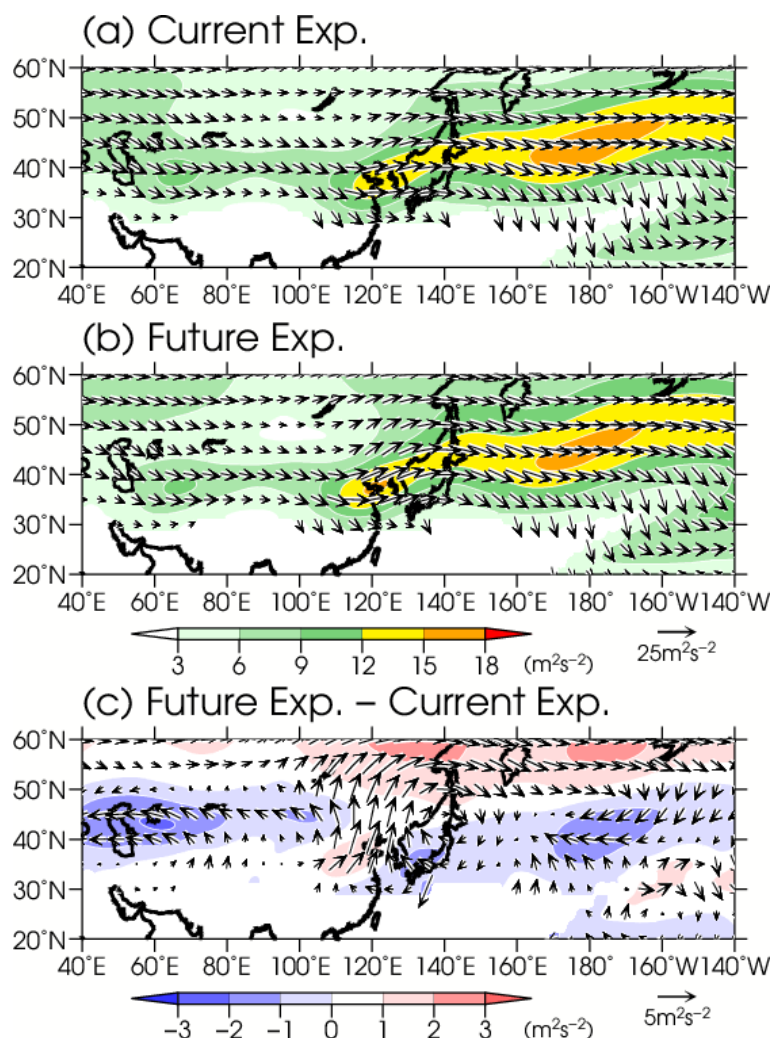
Fig. 9.　Climatology of the horizonal component of WAF (vector; unit: $m^2 s^{-2}$) and the zonal component (shading) at 200 hPa in August for the (a) current, (b) future experiments, and (c) the future change [i.e., (b) minus (a)]. The climatology in (a) and (b) is defined as the 60 year mean of the monthly averaged daily WAFs, and the daily WAFs are derived from the 5 day running mean fields of all ensemble members.

decrease of the RWB frequency over the MNP, through the northward shifted wave propagation over the North Pacific (Figs. 9b, c). The dynamical relationship between the upper-level enhanced stretching deformation (Fig. 5c) and the enhanced northward wave emanation (Fig. 9c) over East Asia will need to be further examined. The other detailed factors of the reduced wave activity, which are suggested by Uchida and Kosaka (2020), are out of scope in this study.

4.3　Convective activities east of the Philippines

Takemura et al. (2017) and Takemura and Mukougawa (2020) showed that the upper-level equatorward

vorticity advection (i.e., high PV intrusion) associated with the RWB east of Japan can contribute to dynamically induced ascent over the subtropical WNP and promotes enhanced convection over the region. Their results suggest that the decreased RWB frequency over the MNP may cause the suppressed convection over the subtropical WNP in the future climate. To assess the above-mentioned hypothesis, the future change of large-scale atmospheric circulations over the subtropical WNP in August is shown in Fig. 10. The 500 hPa ω in August in the current experiment shown in Fig. 10a indicates large-scale upward motion from the Philippines to the east, associated with the enhanced
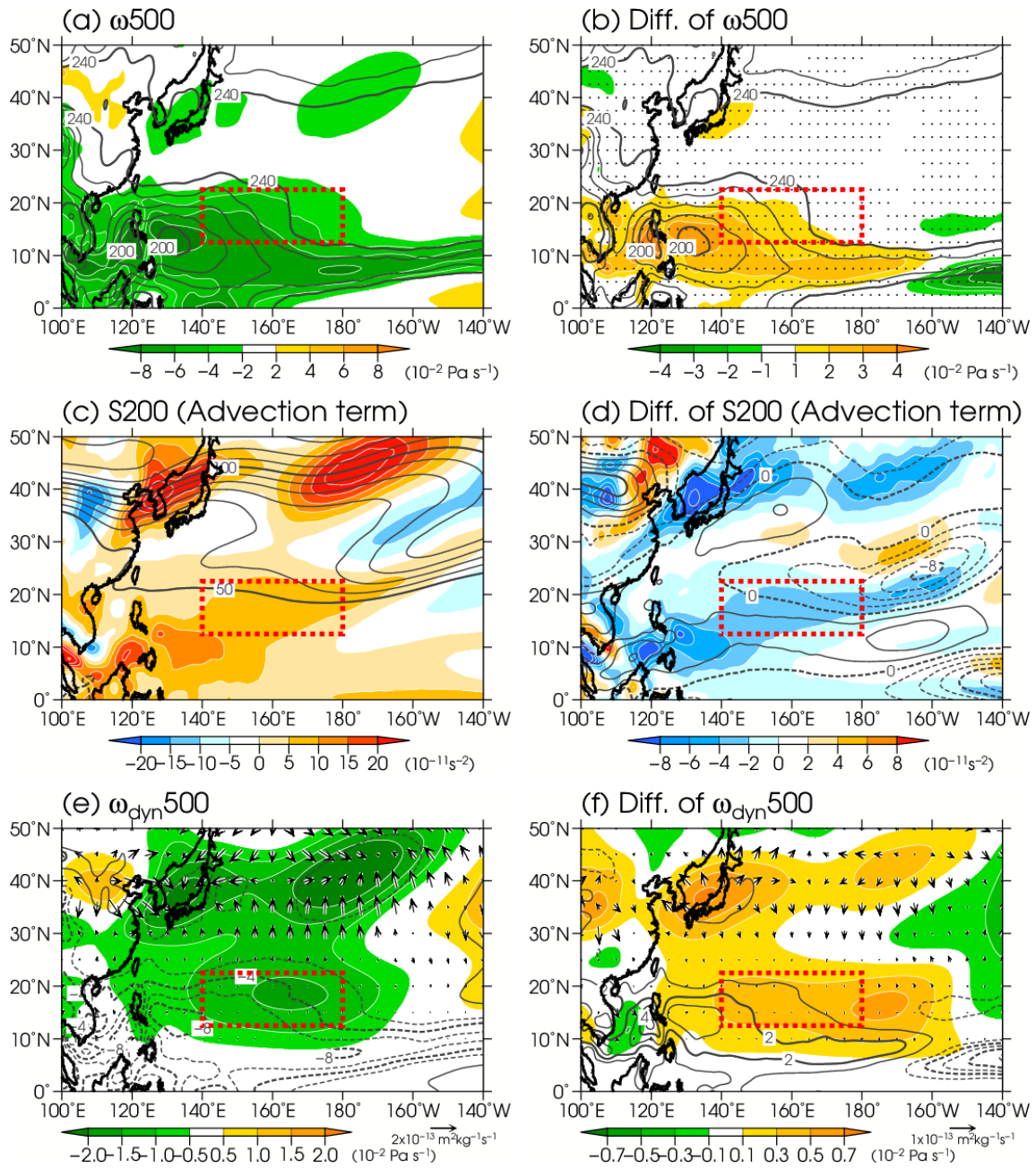
Fig. 10. (a, b) 500 hPa vertical p-velocity (unit: 10^{-2} Pa s^{-1}), (c, d) absolute vorticity advection by 200 hPa horizontal wind (unit: 10^{-11} s^{-2}), and (e, f) dynamically induced vertical motion (ω_{dyn}) north of 5°N at 500 hPa (unit: 10^{-2} Pa s^{-1}) in (left) 60 year climatology of the current experiment and (right) future changes. Contours in (a, b) denote the climatological OLR smaller than 240 W m^{-2} with the intervals of 10 W m^{-2}. Contours in (c) and (d) denote 200 hPa absolute vorticity (unit: 10^{-6} s^{-1}) in the 60 year climatology of the current experiment and the future change with the intervals of 10×10^{-6} s^{-1} and 2×10^{-6} s^{-1}, respectively. Contours and vectors in (e, f) indicate vertical p-velocity and $\boldsymbol{Q}$-vector (unit: m^2 kg^{-1} s^{-1}) at 500 hPa in (e) the 60 year climatology of the current experiment and (f) the future change, respectively. Dots in (b) denote the significant change of 500 hPa vertical p-velocity for all ensemble members of each experiment, with a confidence level of 95 % based on Welch's t-test. The red dashed rectangles denote area (12.5–22.5°N, 140°E–180°) to calculate areal-averaged 500 hPa vertical p-velocity shown in Fig. 12.

Asian summer monsoon. The region of upward motion shown in the negative ω at 500 hPa corresponds to the low OLR in the climatology denoted as contours in Fig. 10a, indicating the validity to assess convective activities over the tropical WNP using ω. The future change of 500 hPa ω shown in Fig. 10b clearly shows positive change east of the Philippines, indicating the significantly suppressed convective activities over the region in the future climate.

Figure 10c shows absolute vorticity advection by horizontal wind at 200 hPa in the current experiment. Here the absolute vorticity advection S is defined as follows:

$$S = -\overline{\boldsymbol{v}} \cdot \nabla (\overline{\zeta} + f), \qquad (5)$$

where $\boldsymbol{v} = (u, v)$ is the horizontal wind vector. The overbars, ζ and f are defined in Eq. (4). The upper-level positive vorticity advection in the current experiment is seen over and south of 20°N east of the Philippines, corresponding to the southwestward extended Mid-Pacific trough from east of the dateline (contours in Fig. 10c). The meridional overturning of the absolute vorticity over the North Pacific (Figs. 7a, 10c) also describes the frequent occurring of RWB over the region. The S at 200 hPa shown as shading in Fig. 10d clearly indicates negative future changes over and south of 20°N east of the Philippines, where the positive S is seen in the current experiment (Fig. 10c). The weakened positive vorticity advection is associated with the weakened extension of the Mid-Pacific trough in the future climate (contours in Fig. 10d), which is resulting from the decreased RWB frequency over the MNP (Fig. 4). The absolute vorticity advection and its future change derived from daily fields in August (not shown) show similar patterns but weaker amplitude than those from monthly averages (Figs. 10c, d). This result indicates that the weakened extension of the Mid-Pacific trough, with not only the daily timescale but also the monthly timescale, is associated with the decreased RWB frequency over the MNP in the future climate. To examine the relationship between the RWB frequency and the extended Mid-Pacific trough, the absolute vorticity advection by 200 hPa horizontal wind regressed onto the areal average of RWB frequency over the MNP for all ensemble members in the current experiment is further shown in Fig. 11. Here, the absolute vorticity advection is derived from the monthly average. The regression of the upper-level absolute vorticity advection, which is scaled to the magnitude of future change in the RWB frequency over the MNP, shows significant positive anomalies (blue shading) from east of the Philippines to the
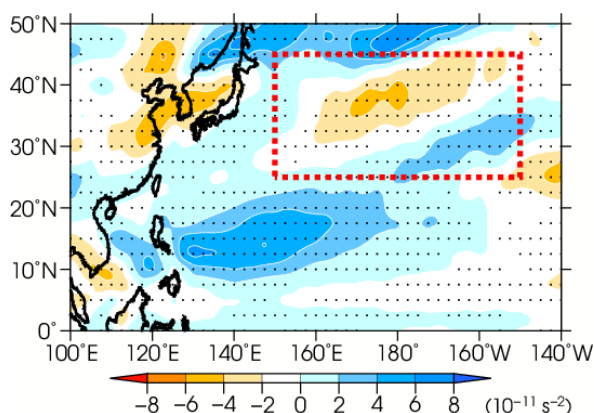

Fig. 11.   Same as Fig. 8 but for absolute vorticity advection by 200 hPa horizontal wind (shading; unit: 10^{-11} s^{-2}) regressed onto areal average of RWB frequency over the MNP (red dashed rectangle). The absolute vorticity advection is derived from the monthly average. The regressed pattern is normalized by the future change of the RWB frequency over the MNP. To highlight the features of absolute vorticity advection associated with the decreased RWB frequency, the order of colors for the shading is reversed from those in Fig. 10d.

south of the MNP. The amplitude of the regressed absolute vorticity advection is comparable with that of the future change (Fig. 10d). These results indicate a contribution of the decreased RWB frequency to the weakened extension of the Mid-Pacific trough through the weakened positive vorticity advection in the future climate.

To assess a dynamical influence of the weakened upper-level vorticity advection (Fig. 10d) on the suppressed large-scale upward motion east of the Philippines (Fig. 10b), vertical motion induced under the quasi-geostrophic balance is diagnosed using ω-equation (e.g., Hoskins et al. 1978; Holton 1992) expressed as follows:

$$\left(\nabla^2 + \frac{f_0^2}{\sigma} \frac{\partial^2}{\partial p^2} \right) \omega_{dyn} \cong \frac{f_0}{\sigma} \frac{\partial}{\partial p} \left[\boldsymbol{v}_g \cdot \nabla \left(\frac{1}{f_0} \nabla^2 \Phi + f \right) \right]$$
$$+ \frac{1}{\sigma} \nabla^2 \left[\boldsymbol{v}_g \cdot \nabla \left(-\frac{\partial \Phi}{\partial p} \right) \right] \quad \text{(6a-1)}$$

$$\cong -\frac{2}{\sigma} \nabla \cdot \boldsymbol{Q} + \frac{f_0}{\sigma} \beta \frac{\partial \boldsymbol{v}_g}{\partial p}, \qquad (6a\text{-}2)$$

$$\boldsymbol{Q} \equiv \left(-\frac{R}{p} \frac{\partial \boldsymbol{v}_g}{\partial x} \cdot \nabla T, \ -\frac{R}{p} \frac{\partial \boldsymbol{v}_g}{\partial y} \cdot \nabla T \right), \qquad (6b)$$

where ω_{dyn} is the dynamically induced vertical p-velocity, f_0 is the reference Coriolis parameter at the latitude of 30°N, f is the Coriolis parameter, $\boldsymbol{Q}$ is the $\boldsymbol{Q}$-vector, $\boldsymbol{v}_g = (u_g, v_g)$ is the geostrophic horizontal wind vector, Φ is the geopotential, and T is the temperature. $\sigma = RT_0 p^{-1} d \ln \theta_0 / dp$ is the static stability, with the gas constant R and the reference potential temperature θ_0, derived from the area-averaged temperature T_0 over the Northern Hemisphere north of 20°N. Equation (6a-1) shows that the ω_{dyn} is balanced with the vertical derivatives of vorticity advection (the first term of the RHS) and thermal advection (the second term of the RHS). The first term of the RHS thus indicates that the upper-level positive vorticity advection as described in Fig. 10c is associated with the negative ω_{dyn} (i.e., ascent). Here, the $\boldsymbol{Q}$-vector and the RHS in Eq. (6a-2) are derived from monthly averages, as in the absolute vorticity advection S (Eq. 5). The ω_{dyn} is calculated, applying a relaxation method to solve the Poisson's equation in Eq. (6a), with meridional boundary conditions at 5°N and the North Pole and vertical ones at pressure levels of the bottom (1000 hPa) and the top (0.5 hPa) given by $\omega_{dyn} = 0$. The ω_{dyn} at 500 hPa in the current experiment shown in Fig. 10e indicates the dynamically induced ascent east of the Philippines, where the northeastern part of the large-scale climatological upward motion is located (dashed contours in Fig. 10e), suggesting the contribution to the enhanced convection over the region.

The dynamical influence of the RWB over the midlatitude WNP on the upward motion east of the Philippines was elucidated by Takemura and Mukougawa (2020) on the basis of a lag composite analysis using the $\boldsymbol{Q}$-vector diagnosis. They indicated that a primary contribution of the upper-level positive vorticity advection associated with the southward intruded high PV accompanied by the RWB to dynamically induced ascent east of the Philippines. Their results support the relationship between the RWB over the MNP and the convective activity east of the Philippines described in this study. The quasi-geostrophic diagnostics in the subtropics, which are the region between the tropics and the midlatitudes, is conducted by Tam and Li (2006) and Funatsu and Waugh (2008), and its validity is also mentioned by Funatsu and Waugh (2008).

The ω_{dyn} at 500 hPa shown as shading in Fig. 10f indicates positive future changes in a wide area east of the Philippines, where the dynamically induced ascent is seen in the current experiment (Fig. 10e). The positive change of the ω_{dyn} thus shows the weakening of dynamically induced ascent associated with the weak-

ened positive vorticity advection as described in Fig. 10d, indicating a partial contribution of the weakened ω_{dyn} to the suppressed convective activities (i.e., the weakened ω) over the region. The contribution rate of the weakened ω_{dyn} will be estimated later in Fig. 12b. The residual component of the suppressed convective activities east of the Philippines, which cannot be explained by the weakened ω_{dyn}, is presumed to be closely associated with the weakened Walker circulation (Fig. 5a) because of increased static stability in tropics in the future climate.

To more quantitatively indicate the aforementioned relationship between the decreased RWB frequency over the MNP and the suppressed dynamically induced vertical motion and the relationship with the convective activities east of the Philippines, their scatter diagrams and histograms for all ensemble members in the current and future experiments are shown in Fig. 12. Here, the 500 hPa ω_{dyn} and ω shown in the scatter diagrams are averaged over the area east of the Philippines (12.5–22.5°N, 140°E–180°; red dashed rectangles in Fig. 10). The scatter diagram shown in Fig. 12a indicates a close relationship of the RWB frequency over the MNP with the 500 hPa ω_{dyn} with a negative correlation coefficient of $R = -0.60$ at a confidence level of 99 %, which is derived from all ensemble members of both the current and future experiments. Their relationships for the current and future experiments are also seen with negative correlation coefficients of $R_C = -0.58$ and $R_F = -0.53$. The scatter diagram shown in Fig. 12b further indicates a close relationship between the ω_{dyn} and ω at 500 hPa with a positive correlation coefficient of $R = +0.61$ at a confidence level of 99 % for all ensemble members of both the current and future experiments. Their relationships for the current and future experiments are also seen with positive correlation coefficients of $R_C = +0.62$ and $R_F = +0.49$. The histograms shown in the upper and right sides of Figs. 12a and 12b further show a clear decreasing shift of the RWB frequency, a weakening shift of dynamically induced ascent, and a weakening shift of large-scale upward motion in the future climate, compared with the current one. The differences in the averaged RWB frequency, ω_{dyn} and ω at 500 hPa between the future experiment and the current experiment shown in the histograms of Figs. 12a and 12b are significant at confidence levels of 99 %.

A ratio of variability in the dynamically induced ascent (ω_{dyn}) to that in the large-scale upward motion (ω) at 500 hPa can be calculated from the slope of their regression line derived from all ensemble

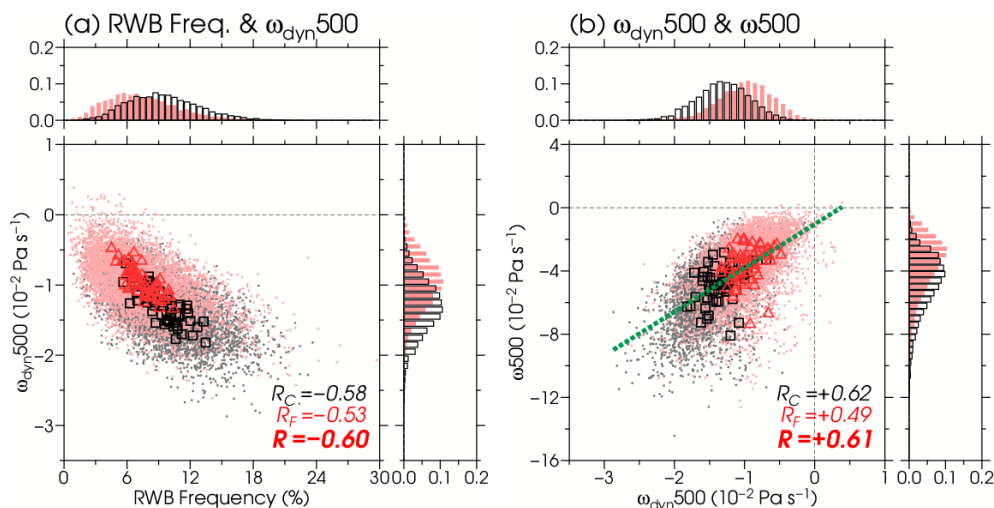Fig. 12.   Scatter diagrams between (a) the RWB frequency (X-axis) and dynamically induced vertical motion (ω_{dyn}) at 500 hPa (unit: 10^{-2} Pa s^{-1}) averaged over the area east of the Philippines (EOP; 12.5–22.5°N, 140°E–180°) and (b) the ω_{dyn} and 500 hPa vertical p-velocity (ω) (unit: 10^{-2} Pa s^{-1}) averaged over the EOP. The gray and light red dots denote all ensemble members in the current and future experiments, respectively. The black squares and red triangles denote the ensemble mean in the current and future experiments, respectively. The correlation coefficients between the X- and Y-components in all ensemble members of the current (R_C) and future (R_F) experiments and their combination (R) are shown at the bottom right. The green dashed line in (b) denotes a regression line derived from all ensemble members of the current and future experiments. The upper and right sides of each scatter diagram show histograms of the X- and Y-components, respectively. The black boxes and red bars indicate the histograms of all ensemble members in the current and future experiments. The histograms are normalized by each sample number.

members in the current and future experiments (green dashed line in Fig. 12b). The ratio derived from the areal averages over the area east of the Philippines (red dashed rectangles in Fig. 10) is statistically estimated as approximately 36 %, indicating a non-negligible relationship of the weakened dynamically induced ascent with the suppressed convective activities east of the Philippines.

The results of diagnosis using the ω-equation and correlation analysis described in this subsection indicate the contribution of the decreased RWB frequency over the MNP to the suppressed convective activities east of the Philippines. The significantly suppressed convection near the Philippines (Fig. 10b) is consistent with the reduced frequency of the PJ pattern with cyclonic (anticyclonic) circulation anomalies around the Philippines (Japan), which is indicated by Kosaka and Nakamura (2011).

5.   Concluding remarks

The future change of RWB frequency over the MNP in August and the related features of the large-scale atmospheric circulation were examined using the

d4PDF dataset, which is the large-ensemble simulations with a global circulation model. The correlation with the reanalysis indicated that the RWB frequency over the MNP in the current experiment could show the relationship to the ENSO as JRA-55. The RWB frequency over the MNP in the future climate showed a significant decrease compared with that in the current climate. The upper-level atmospheric circulation in the future climate indicated the significant weakening of large-scale divergence from South to Southeast Asia and the consequent southward shifted Asian jet. The decreased RWB frequency over the MNP is associated with the modulated Asian jet, through the reduced diffluence and deceleration of the jet in the basic state over the region. The reduced Rossby wave propagation over Eurasia and the North Pacific in midlatitudes was also clear in the future climate and also consistent with the decreased RWB frequency over the MNP. The results of correlation analysis in the current and future experiments indicated that the decreased RWB frequency over the MNP is related to the suppressed convective activities east of the Philippines. The diagnosis using ω-equation further showed

the process in the impact of the decreased RWB frequency on the suppressed convective activities in the future climate, through the weakened extension of the Mid-Pacific trough and the consequent weakening of dynamically induced ascent east of the Philippines. The suppressed large-scale upward motion shown in this study suggests a consistent condition with the decreased number of tropical cyclones and their seeds (e.g., Yoshida et al. 2017; Sugi et al. 2020), although these future changes cannot be fully explained from those of ω at 500 hPa.

As noted in Section 3, the underestimated and eastward shifted RWB frequency reproduced in the current experiment compared with the reanalysis may have an impact on the quantitative assessment for the future change of the frequency. Scaife et al. (2010) showed a largely improved reproducibility of the blocking frequency, resulting from the corrected climatological mean bias of geopotential height in their model. According to the result of Scaife et al. (2010), a physical understanding of the reproducibility of the RWB in the climate models will provide us further confidences in the future changes of the RWB frequency. Although the future changes shown in this study were estimated from a large-ensemble simulation with 100 members using a single climate model, the statistical relationship with the vertical p-velocity shown in Fig. 12 may be somewhat affected by the cumulus parameterization scheme in the model.

Although the interannual variability of SSTs in the future experiment is the same as in the current one as described in Section 2, the modulation of ENSO associated with a warmer climate was indicated by Cai et al. (2018). According to the close relationship between the RWB frequency over the MNP and the ENSO (Fig. 3), the RWB frequency may also be influenced by the modulated ENSO under the warmer climate, which is not included in the results of the future experiment.

On the basis of the aforementioned discussions, further diagnosis of the large-ensemble simulation using the other schemes or climate models with the other boundary conditions will be desired to perform a more rigorous and quantitative assessment for the future changes of the RWB frequency.

Acknowledgments

References

Abatzoglou, J. T., and G. Magnusdottir, 2006: Planetary wave breaking and nonlinear reflection: Seasonal cycle and interannual variability. *J. Climate*, **19**, 6139–6152.

Bluestein, H. B., 1992: *Synoptic-Dynamic Meteorology in Midlatitudes*. Oxford University Press, 448 pp.

Bowley, K. A., J. R. Gyakum, and E. H. Atallah, 2019: A new perspective toward cataloging Northern Hemisphere Rossby wave breaking on the dynamic tropopause. *Mon. Wea. Rev.*, **147**, 409–431.

Cai, W., G. Wang, B. Dewitte, L. Wu, A. Santoso, K. Takahashi, Y. Yang, A. Carréric, and M. J. McPhaden, 2018: Increased variability of eastern Pacific El Niño under greenhouse warming. *Nature*, **564**, 201–206.

Colucci, S. J., 2001: Planetary-scale preconditioning for the onset of blocking. *J. Atmos. Sci.*, **58**, 933–942.

Colucci, S. J., and T. L. Alberta, 1996: Planetary-scale climatology of explosive cyclogenesis and blocking. *Mon. Wea. Rev.*, **124**, 2509–2520.

de Vries, H., T. Woollings, J. Anstey, R. J. Haarsma, and W. Hazeleger, 2013: Atmospheric blocking and its relation to jet changes in a future climate. *Climate Dyn.*, **41**, 2643–2654.

Enomoto, T., 2004: Interannual variability of the Bonin high associated with the propagation of Rossby waves along the Asian jet. *J. Meteor. Soc. Japan*, **82**, 1019–1034.

Enomoto, T., B. J. Hoskins, and Y. Matsuda, 2003: The formation mechanism of the Bonin high in August. *Quart. J. Roy. Meteor. Soc.*, **129**, 157–178.

Funatsu, B. M., and D. W. Waugh, 2008: Connections between potential vorticity intrusions and convection in the eastern tropical Pacific. *J. Atmos. Sci.*, **65**, 987–1002.

Hirahara, S., H. Ohno, Y. Oikawa, and S. Maeda, 2012: Strengthening of the southern side of the jet stream and delayed withdrawal of Baiu season in future climate. *J. Meteor. Soc. Japan*, **90**, 663–671.

Hirahara, S., M. Ishii, and Y. Fukuda, 2014: Centennial-scale sea surface temperature analysis and its uncertainty. *J. Climate*, **27**, 57–75.

Holton, J. R., 1992: *An Introduction to Dynamic Meteorology. 3rd Edition*. Academic Press, 511 pp.

Horinouchi, T., S. Matsumura, T. Ose, and Y. N. Takayabu, 2019: Jet–precipitation relation and future change

of the mei-yu–baiu rainband and subtropical jet in CMIP5 coupled GCM simulations. *J. Climate*, **32**, 2247–2259.

Hoskins, B. J., I. Draghici, and H. C. Davies, 1978: A new look at the ω-equation. *Quart. J. Roy. Meteor. Soc.*, **104**, 31–38.

Imada, Y., S. Maeda, M. Watanabe, H. Shiogama, R. Mizuta, M. Ishii, and M. Kimoto, 2017: Recent enhanced seasonal temperature contrast in Japan from large ensemble high-resolution climate simulations. *Atmosphere*, **8**, 57, doi:10.3390/atmos8030057.

Imada, Y., M. Watanabe, H. Kawase, H. Shiogama, and M. Arai, 2019: The July 2018 high temperature event in Japan could not have happened without human-induced global warming. *SOLA*, **15A**, 8–12.

Kobayashi, S., Y. Ota, Y. Harada, A. Ebita, M. Moriya, H. Onoda, K. Onogi, H. Kamahori, C. Kobayashi, H. Endo, K. Miyaoka, and K. Takahashi, 2015: The JRA-55 reanalysis: General specifications and basic characteristics. *J. Meteor. Soc. Japan*, **93**, 5−48.

Kosaka, Y., and H. Nakamura, 2006: Structure and dynamics of the summertime Pacific–Japan teleconnection pattern. *Quart. J. Roy. Meteor. Soc.*, **132**, 2009–2030.

Kosaka, Y., and H. Nakamura, 2011: Dominant mode of climate variability, intermodel diversity, and projected future changes over the summertime western North Pacific simulated in the CMIP3 models. *J. Climate*, **24**, 3935–3955.

Kosaka, Y., H. Nakamura, M. Watanabe, and M. Kimoto, 2009: Analysis on the dynamics of a wave-like teleconnection pattern along the summertime Asian jet based on a reanalysis dataset and climate model simulations. *J. Meteor. Soc. Japan*, **87**, 561–580.

Liebmann, B., and C. A. Smith, 1996: Description of a complete (interpolated) outgoing longwave radiation dataset. *Bull. Amer. Meteor. Soc.*, **77**, 1275–1277.

Lorenz, D. J., and E. T. DeWeaver, 2007: Tropopause height and zonal wind response to global warming in the IPCC scenario integrations. *J. Geophys. Res.*, **112**, D10119, doi:10.1029/2006JD008087.

Lu, R.-Y., J.-H. Oh, and B.-J. Kim, 2002: A teleconnection pattern in upper-level meridional wind over the North African and Eurasian continent in summer. *Tellus*, **54**, 44–55.

Mak, M., and M. Cai, 1989: Local barotropic instability. *J. Atmos. Sci.*, **46**, 3289–3311.

Matsueda, M., and H. Endo, 2017: The robustness of future changes in Northern Hemisphere blocking: A large ensemble projection with multiple sea surface temperature patterns. *Geophys. Res. Lett.*, **44**, 5158–5166.

Mizuta, R., H. Yoshimura, H. Murakami, M. Matsueda, H. Endo, T. Ose, K. Kamiguchi, M. Hosaka, M. Sugi, S. Yukimoto, S. Kusunoki, and A. Kitoh, 2012: Climate simulations using MRI-AGCM3.2 with 20-km grid. *J. Meteor. Soc. Japan*, **90A**, 233–258.

Mizuta, R., A. Murata, M. Ishii, H. Shiogama, K. Hibino, N.

Mori, O. Arakawa, Y. Imada, K. Yoshida, T. Aoyagi, H. Kawase, M. Mori, Y. Okada, T. Shimura, T. Naga-tomo, M. Ikeda, H. Endo, M. Nosaka, M. Arai, C. Takahashi, K. Tanaka, T. Takemi, Y. Tachikawa, K. Temur, Y. Kamae, M. Watanabe, H. Sasaki, A. Kitoh, I. Takayabu, E. Nakakita, and M. Kimoto, 2017: Over 5,000 years of ensemble future climate simulations by 60-km global and 20-km regional atmospheric models. *Bull. Amer. Meteor. Soc.*, **98**, 1383–1398.

Nitta, T., 1987: Convective activities in the tropical western Pacific and their impact on the Northern Hemisphere summer circulation. *J. Meteor. Soc. Japan*, **65**, 373–390.

Pelly, J. L., and B. J. Hoskins, 2003: A new perspective on blocking. *J. Atmos. Sci.*, **60**, 743–755.

Postel, G. A., and M. H. Hitchman, 1999: A climatology of Rossby wave breaking along the subtropical tropopause. *J. Atmos. Sci.*, **56**, 359–373.

Postel, G. A., and M. H. Hitchman, 2001: A case study of Rossby wave breaking along the subtropical tropopause. *Mon. Wea. Rev.*, **129**, 2555–2569.

Scaife, A. A., T. Woollings, J. Knight, G. Martin, and T. Hinton, 2010: Atmospheric blocking and mean biases in climate models. *J. Climate*, **23**, 6143–6152.

Scaife, A. A., D. Copsey, C. Gordon, C. Harris, T. Hinton, S. Keeley, A. O'Neill, M. Roberts, and K. Williams, 2011: Improved Atlantic winter blocking in a climate model. *Geophys. Res. Lett.*, **38**, L23703, doi:10.1029/2011GL049573.

Sooraj, K. P., P. Terray, and M. Mujumdar, 2015: Global warming and the weakening of the Asian summer monsoon circulation: Assessments from the CMIP5 models. *Climate Dyn.*, **45**, 233–252.

Sugi, M., A. Noda, and N. Sato, 2002: Influence of the global warming on tropical cyclone climatology: An experiment with the JMA global model. *J. Meteor. Soc. Japan*, **80**, 249–272.

Sugi, M., Y. Yamada, K. Yoshida, R. Mizuta, M. Nakano, C. Kodama, and M. Satoh, 2020: Future changes in the global frequency of tropical cyclone seeds. *SOLA*, **16**, 70–74.

Takaya, K., and H. Nakamura, 2001: A formulation of a phase-independent wave activity flux for stationary and migratory quasigeostrophic eddies on a zonally varying basic flow. *J. Atmos. Sci.*, **58**, 608–627.

Takemura, K., Y. Kubo, and S. Maeda, 2017: Relation between a Rossby wave-breaking event and enhanced convective activities in August 2016. *SOLA*, **13**, 120–124.

Takemura, K., and H. Mukougawa, 2020: Dynamical relationship between quasi-stationary Rossby wave propagation along the Asian jet and Pacific–Japan pattern in boreal summer. *J. Meteor. Soc. Japan*, **98**, 169–187.

Takemura, K., H. Mukougawa, and S. Maeda, 2020: Large-scale atmospheric circulation related to frequent

Rossby wave breaking near Japan in boreal summer. *J. Climate*, **33**, 6731–6744.

Tam, C.-Y., and T. Li, 2006: The origin and dispersion characteristics of the observed tropical summertime synoptic-scale waves over the western Pacific. *Mon. Wea. Rev.*, **134**, 1630–1646.

Tokyo Climate Center, 2020: Download El Niño monitoring indices. Japan Meteorological Agency. https://ds.data.jma.go.jp/tcc/tcc/products/elnino/index/index.html. (Accessed on 25 June 2021).

Uchida, Y., and Y. Kosaka, 2019: Modulation of the Silk Road pattern due to global warming in d4PDF. Preprints, *the MSJ Annual Scientific Meetings (Autumn 2019)*. 470 pp (in Japanese).

Uchida, Y., and Y. Kosaka, 2020: Modulation of the Silk Road pattern due to global warming and its factors. Preprints, *the MSJ Annual Scientific Meetings (Spring 2020)*. 104 pp (in Japanese).

Wakabayashi, S., and R. Kawamura, 2004: Extraction of major teleconnection patterns possibly associated with the anomalous summer climate in Japan. *J. Meteor. Soc. Japan*, **82**, 1577–1588.

Yoshida, K., M. Sugi, R. Mizuta, H. Murakami, and M. Ishii, 2017: Future changes in tropical cyclone activity in high-resolution large-ensemble simulations. *Geophys. Res. Lett.*, **44**, 9910–9917.